JOURNAL OF AIRCRAFT
Vol. 48, No. 3, May–June 2011

Improvement to Patched Grid Technique with High-Order Conservative Remapping Method

Yufei Zhang,* Haixin Chen,† and Song Fu‡
Tsinghua University, 100084 Beijing, People's Republic of China

DOI: 10.2514/1.C031093

A conservative remapping method is developed to improve the accuracy of data exchange on the patched (mismatched) grid interface. Linear and quadratic polynomials are tested for the reconstruction of the conservative variables on the interface. Remapping methods with different accuracies are compared. Results show that the combination of the linear reconstruction and the weighted essentially nonoscillatory stencil selection has the best balance of accuracy and efficiency. Numerical study of the DLR-F4 wing–body combination with a mending plate patched on the wing upper surface is carried out with the in-house code NSAWET. A sharp pressure jump and an approximate one-count drag increment brought by the plate can be captured.

Nomenclature

$A_{j,k,m,n}$	=	section of area of cell (j, k) in overlap with cell (m, n)
C_d	=	drag coefficient
$C_{d,f}$	=	friction drag coefficient
$C_{d,p}$	=	pressure drag coefficient
C_l	=	lift coefficient
C_p	=	pressure coefficient
FLUX	=	flux between interfaces
h	=	conservative variables
IS	=	smoothness measurement of cell
Ma	=	Mach number
M_z	=	pitching moment
Re	=	Reynolds number
$\bar{U}$	=	mean flow conservative variables in a cell
α_i	=	weight for ith stencil

I. Introduction

COMPUTATIONAL fluid dynamics (CFD) have been widely applied in the design of aircraft to reduce the wind-tunnel test costs and the design cycle time. Although the unstructured and Cartesian grid approaches developed rapidly in recent years, the multiblock structural grid approach is still showing its advantages in computational efficiency, memory occupation, and (very often) better numerical simulation accuracy. Compared with the unstructured grid approach, the major drawbacks of the conventional one-to-one matched structural grid method are its difficulty in handling complex geometry and inconvenience in local grid refinement.

The patched grid technique is a zonal structural grid method. Unlike the one-to-one matched grid approach, two neighboring grid blocks need not be identical at their interface. Hence, the patched grid technique can easily decompose the flowfield into regions with different grid topologies and densities. In [1,2], the flowfield around an airfoil is divided into two-dimensional (2-D) and three-dimensional (3-D) regions. A much denser grid can be adapted in the 3-D region. Also, in the window-embedment technology proposed by Chen and Fu [3], with the patched grid technique, the multiscale complex aerodynamic geometry could be easily decomposed into simple parts. The overall grids can then be reassembled with grid blocks from each part [3,4].

Since the neighboring two grid blocks always have clean interfaces [5], it is easier for the patched grid to maintain better conservation than, for instance, a chimera grid in the computation. The patched grid technique was proposed by Rai [6] for the finite difference method and extended to the finite volume method by Walters et al. [7]. Rai [6] used a piecewise-constant reconstruction on the interface, which gives first-order accuracy and has a stairlike effect when interpolating from coarse to fine grids. Thomas et al. [8] proposed a second-order-accuracy patched grid technique with a piecewise linear reconstruction on the interface to eliminate the stairlike effect. Lerat and Wu [9] developed a conservative and unconditionally stable patched grid algorithm. The method is linearly equivalent to an area-weighted interpolation of the state vector [10]. Benkenida et al. [10] developed a patched grid flux computation method and pointed out that the conservation of flux is equal to the area-weighted interpolation of the state vector in the central finite volume scheme. Yang et al. [11] applied the patched grid technique to the Roe FDS method, with MUSCL interpolation in the computation of casing treatment of the compressor rotor. Esquieu [12,13] used the patched grid technique on the drag prediction of wing–body configuration successfully.

In the present work, the patched grid technique is further developed based on the previous work of Chen and Fu [3] and Chen et al. [14]. The overlapped area-weighted remapping [3] proposed there is, in fact, upgraded with linear and quadratic polynomials reconstruction [15]. Essentially nonoscillatory (ENO) [15,16] and weighted ENO (WENO) [17] methods are employed to select or combine the appropriate stencil(s) to preserve the stability and accuracy of the remapping.

The present improved patched grid technique is applied in the computational study of the aerodynamic performance of a repaired wing on which a thin plate for the repair had been patched. Although the mending plate is thin, it may bring unknown aerodynamic effects to the wing in flight conditions. These effects need to be evaluated, especially for civil aircraft, as they are sensitive to changes in drag and moment. However, the numerical simulation of such a mending plate with conventional CFD can be difficult for three reasons:

1) The tiny protruding height needs to be resolved with a very fine grid, although such a fine grid is neither necessary nor acceptable to the simulation of the whole configuration.

2) The edges of the plate may not be aligned with the chord or the leading/trailing edge of the wing, bringing difficulties to the high-quality grid generation.

Presented as Paper 2010-0167 at the 48th AIAA Aerospace Sciences Meeting Including the New Horizons Forum and Aerospace Exposition, Orlando, FL, 4–7 January 2010; received 2 May 2010; revision received 9 November 2010; accepted for publication 30 December 2010.

*Postdoctoral Research Assistant, School of Aerospace Engineering.
†Associate Professor, School of Aerospace Engineering. Senior Member AIAA.
‡Professor, School of Aerospace Engineering; fs-dem@tsinghua.edu.cn. Associate Fellow AIAA.

3) The magnitude of the drag increment is so small that the CFD method needs to have extremely high accuracy and resolution. The window-embedment technology, incorporated with the patched grid technique, provides a powerful yet easy tool for such a problem; the data exchange at the patched grid interface requires very good accuracy.

II. Patched Grid Technique

A. Flux Computation on Mismatched Interface

The core of the patched grid technique is the realization of the data exchange at the mismatched multiblock grid interfaces. For simplicity, the data exchange can be explained in the 2-D sketch map in Fig. 1 [3], which can be viewed as the side view of a simplified mismatched interface. Grid blocks 1 and 2, patched on the interface, are drawn by dashed and solid lines, and they are labeled as indices (j, k) and (m, n), respectively. When using a phantom grid technique at the interface, a dummy grid cell $(j, k+1)$ can be created for the cell (j, k) in block 1. As an example, for the Jameson cell-centered finite volume method with a piecewise-constant reconstruction on the mismatched surface, the flux on the cell surface $(j, k+\frac{1}{2})$ can be written as

$$\begin{aligned}\mathrm{FLUX}_{(j,k+\frac{1}{2})} &= \frac{(\mathbf{h}_{j,k}+\mathbf{h}_{j,k+1})}{2}A_{j,k+\frac{1}{2}} \\ &= \frac{(\mathbf{h}_{j,k}+\mathbf{h}_{j,k+1,m+1,n})}{2}A_{j,k,m+1,n}+\frac{(\mathbf{h}_{j,k}+\mathbf{h}_{j,k+1,m,n})}{2}A_{j,k,m,n} \\ &= \frac{(\mathbf{h}_{j,k}+\mathbf{h}_{m+1,n})}{2}A_{j,k,m+1,n}+\frac{(\mathbf{h}_{j,k}+\mathbf{h}_{m,n})}{2}A_{j,k,m,n} \qquad (1)\end{aligned}$$

where $\mathbf{h}$ denotes a conservative variable and the subscript indicates the indices of the grid cell; $A_{j,k,m,n}$ is the section of the area of the cell (j, k) in overlap with the cell (m, n).

Following the method proposed by Benkenida et al. [10], showing the conservation of flux equal to the area-weighted interpolation of the state vector in the ghost cell, here, a general form for the conservative variables in the dummy cells can be derived. With N referring to the number of cells in block 2 that overlaps with the cell (j, k), the $\mathbf{h}$ in the dummy cell $(j, k+1)$ can be expressed as

$$\mathbf{h}_{j,k+1} = \sum_{l=1}^{N} \mathbf{h}_{(m,n)_l} \frac{A_{j,k,(m,n)_l}}{A_{j,k+\frac{1}{2}}} \qquad (2)$$

Thus, the flow variables in the dummy cells, which are needed by the interface flux computation of block 1 cells, are remapped from the parameters in block 2 boundary cells weighted by their overlapping area. From the deduction procedure, it is easy to understand that when incorporated into the cell-centered finite volume method or other convective schemes, this technique could guarantee the global flux conservation on the mismatched interfaces.

The conservative remapping method has two steps. When the flow data are being transferred from block 2 to block 1, the first step deals with the variable reconstruction in block 2 boundary grid cells, and the second step rebuilds the variables for block 1 ghost cells.

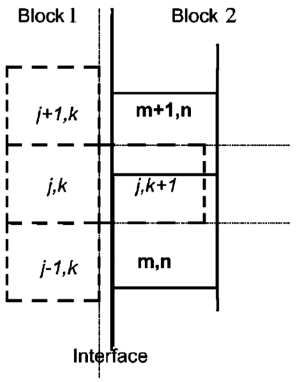

Fig. 1 Side view sketch of a simplified mismatched grid interface.

B. Reconstruction on Block 2 Side

In Chen and Fu's previous version of the patched grid technique [3], the conservative variables are assumed constant in each grid cell, called piecewise-constant (or zeroth order) reconstruction. Although such a simplification is commonly used in finite volume spatial schemes with an accuracy order no higher than two, and it makes the flow information exchange naturally conservative and monotone, the remapping can only be first-order accurate. Such a method is excessively diffusive and of low resolution and fidelity, especially when flowfield data are remapped between two grids for which the density differs significantly at the interface. Moreover, it may cause an unwanted stairlike effect in the results [8].

To increase the remapping accuracy while keeping the conservation, piecewise linear or quadratic reconstruction in grid cells can be used [15,16,18]. The conservative remapping method is originally proposed in moving grid or grid adaptive refinement applications. When the grid is moved, deformed, or refined, the conservative variable in the old grid could be remapped onto the new grid.

Two grid surfaces discretized from the same curved surface will hardly be identical if the distributions of the grid points are different. Researchers have done some work for the curved surfaces interpolation to approximately preserve the flux conservation [8]. If the conservation and accuracy need to be strictly guaranteed, the remapping requires the interfaces to be planar. For simplicity, reconstruction on the X-Y plane is considered here. If the patch surface is a spatial plane, a proper projection is needed.

1. *Polynomial Reconstructions*

For an arbitrary variable U (can be state vector or conservative variables), the following polynomials can be used for reconstructions in a grid cell [15,16,18]:

1) The constant polynomial is $U(x, y) = \bar{U}$.
2) The linear polynomial is $U(x, y) = q_0 + q_x x + q_y y$.
3) The quadratic polynomial is

$$U(x, y) = q_0 + q_x x + q_y y + q_{xy} xy + q_{xx} x^2 + q_{yy} y^2$$

Here, $\bar{U}$ is the mean value in the cell,

$$\bar{U} = \iint_{\text{cell}} U(x, y)\,\mathrm{d}x\,\mathrm{d}y \Big/ \iint_{\text{cell}} \mathrm{d}x\,\mathrm{d}y$$

and q_0, q_x, q_y, q_{xy}, q_{xx}, and q_{yy} are coefficients to be determined.

The coefficients in the linear and quadratic reconstructions can be determined by solving the following equation:

$$\overline{U(x, y)}_i = \bar{U}_i \qquad (3)$$

This equation means that the value at a cell center is equal to the mean value of the cell, or the integral value of the polynomial distribution in a cell is equal to the mean value multiplying the cell area. It is obvious that three equations need to be solved in three cells to get the three unknown coefficients for the linear reconstruction in a cell. In other words, the stencil needs three cells. As to the quadratic reconstruction, a six-cell stencil is needed.

2. *Selection of Stencils*

For the reconstruction on an individual grid cell (for example, cell 0 in Figs. 2 and 3), the number of the neighboring cells, plus the cell itself, is usually larger than the stencil size. This makes a large number of combinations of the grid cells, which can form different stencils. However, as the input to the ENO selection or the WENO combination, which will be discussed in the next subsection, the stencils must be screened first to get a good set of candidates. As in [16,17], the following properties are concluded for a good stencil set:

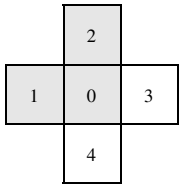

Fig. 2 Selection of stencil points in linear reconstruction.

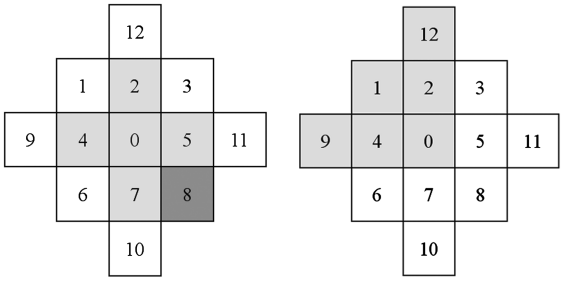

Fig. 3 Selection of stencil points in quadratic reconstruction.

1) For the nonsingular property, the equations can not be singular; that is, for linear reconstruction, the three stencil points cannot be in line, and for quadratic reconstruction, the six stencil points cannot be on only one or two line(s).

2) For the symmetry property, in the set, a stencil must be able to find peers symmetrical to it in both of the two index directions. This is to avoid the unbalanced or biased sourcing of flow information for the remapping. Moreover, the stencil set needs to guarantee that a unique solution of the polynomial coefficients can be attained when processing the same mesh with a sweeping of the grid index in a different direction.

3) For the upwind property, for the remapping of flow discontinuity across the cell reconstructed, there should be at least one stencil for which the cells are all at one side of the discontinuity.

As in Fig. 2, for the linear reconstruction, if we want to reconstruct the variable distribution in grid cell 0, the four neighbor cells can be stencil points (Fig. 2). According to the nonsingular property, $\{0, 1, 2\}$ could be a good stencil. Considering the symmetry property, $\{0, 2, 3\}$, $\{0, 3, 4\}$, and $\{0, 1, 4\}$ should also be included in the candidate stencil set. The upwind property can be satisfied automatically in this case. This four-stencil set can lead to four groups of coefficients $\{q_{0i}, q_{xi}, q_{yi}, i = 1 \sim 4\}$.

For quadratic reconstruction, six equations need to be solved. The 12 neighbor cells can be the candidate stencil points (Fig. 3). Many more combinations are eligible for the stencil set. Here, the following two steps are adopted for the selection:

1) Choose the four nearest neighbor cells $\{2, 4, 5, 7\}$ and a corner neighbor $\{8\}$ (Fig. 3a) as a stencil. According to the symmetry property, replacing $\{8\}$ by $\{1\}$, $\{3\}$, or $\{6\}$ leads to three other stencils.

2) To satisfy the upwind property (stencil illustrated in Fig. 3b), $\{0, 1, 2, 4, 9, 12\}$ should be included in the set. According to the symmetry property, $\{0, 2, 3, 5, 11, 12\}$, $\{0, 5, 7, 8, 10, 11\}$, and $\{0, 4, 6, 7, 9, 10\}$ should also be included.

Thus, eight candidate stencils are obtained. Eight groups of coefficients can be derived, designated as $q_{0i}, q_{xi}, q_{yi}, q_{xyi}, q_{xxi}, q_{yyi}$, $i = 1 \sim 8$.

Generally, linear reconstruction needs to solve four groups of linear equations with three unknowns, and quadratic reconstruction needs to solve eight groups of linear equations with six unknowns. When using the Gaussian elimination method, the latter requires about 12 times more CPU costs than the former.

3. Essentially Nonoscillatory and Weighted Essentially Nonoscillatory Strategies

While the conservation of the remapping method is critical to the calculation of the discontinuity across the mismatched interface, its monotonicity is important to the remapping of the discontinuity on the interface. The monotonicity suggests that no new peak point is introduced in the interpolation process. As a strong constraint for the stability of a numerical scheme, the monotonicity often decreases the scheme accuracy. In the piecewise-constant reconstruction, the monotonicity is inherently satisfied. However, the higher-order remapping methods need to carefully balance the monotonicity and accuracy, especially when discontinuity occurs at the interface.

In the present work, the ENO and WENO strategies are adopted to select one stencil or make a combination of the stencils from the stencil set to get the proper coefficients for the polynomial reconstruction. ENO and WENO are strategies frequently employed for reconstruction in multidimensional CFD spatial schemes [17,19,20]. In ENO and WENO, the monotonicity is not strictly guaranteed. However, the advantage is that they can preserve the scheme's accuracy well while smoothly capturing the discontinuity in the field. The numerical stabilities of ENO and WENO schemes have been widely verified in research. However, for the high-order multidimensional applications, the selection of the best ENO stencil or the best WENO combination of the stencils is a very interesting research topic.

The ENO strategy can be used in an interpolation algorithm to achieve the required high accuracy while preserving oscillation-free results through making the interpolation based on the local smoothest stencil [21]. In the present approach, ENO selects the stencil with $\min(|q_{xi}| + |q_{yi}|)$ for linear reconstruction and $\min(|q_{xyi}| + |q_{xxi}| + |q_{yyi}|)$ for quadratic reconstruction. ENO interpolation is uniformly highly accurate up to the discontinuity, and it is robust. However, it does have some drawbacks. One problem is the floating selection of stencil does not make full use of all the stencils, and the final choice may be abruptly changed by a roundoff perturbation. Another problem is the cost relating to too much computation time on logical judgments. WENO interpolation can remedy these drawbacks. A convex combination of all the candidate stencils is used; the weights are decided by the smoothness of the local flowfield as well as each individual stencil.

In the present paper, the WENO strategy introduced in [21] is adapted. The basic idea is as follows:

1) A smoother stencil has higher accuracy for the polynomial and is assigned a higher weight.

2) The stencil with its points closer to the reconstructed target point takes a higher weight. In this way, a factor α_i for the ith stencil is calculated as follows:

$$\alpha_i = 1/(\varepsilon + IS^m \cdot d^l) \tag{4}$$

where $\varepsilon = 10^{-5}$,

$$IS = \sum_{k=0}^{n-1} (U_k - U_{\text{aver}})^2$$

$$d = \sum_{k=1}^{n-1} \sqrt{(x_k - x_0)^2 + (y_k - y_0)^2}$$

and n is the number of the points in the stencil, which is three for the linear reconstruction and six for the quadratic reconstruction. IS is the smoothness measurement of the stencil, d is the distance factor, and m and l are the powers to adjust the relative influence of smoothness and distance. Here, we set $m = 2$, and $l = 1$.

According to the size of stencil set, for the linear reconstruction, $i = 1, 4$. For the quadratic reconstruction, $i = 1, 8$; the weight of each stencil is normalized by $\beta_i = \alpha_i / \sum \alpha_i$. Take the quadratic reconstruction, for example; the resulted distribution of U in the target cell is

$$U = \sum_{i=1}^{8} \beta_i (q_{0i} + q_{xi}x + q_{yi}y + q_{xyi}xy + q_{xxi}x^2 + q_{yyi}y^2) \tag{5}$$

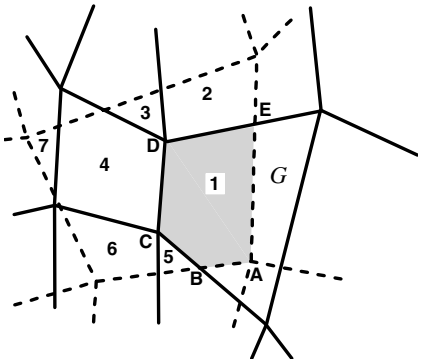

Fig. 4 Sketch of the remapping on a mismatched interface.

C. Rebuilding for Block 1 Side

As shown in Fig. 4, a rebuilding process is needed for the dashed mesh (in block 1) to obtain the ghost cell values from the solid mesh. The dashed target mesh cell fully or partially covers seven solid cells. The rebuilt cell-center value for the dashed grid cell is calculated by

$$U = \sum_{i=1}^{7} \bar{U}_i A_i / \sum_{i=1}^{7} A_i$$

The shadowed area, ABCDE, or area 1 is in the solid cell G. This area should calculate its contribution to the dashed cell by integrating the cell G reconstruction formula. The integration on this pentagon can be replaced by summing up the contributions from its boundary segments:

$$\bar{U}_1 A_1 = Q_{AB} + Q_{BC} + Q_{CD} + Q_{DE} + Q_{EA} \tag{6}$$

where $\bar{U}_1$ is the mean value in the shadowed region, A_1 is the area, and Q_{AB} is the contribution from the segment AB. Take the quadratic distribution as an example:

$$\begin{aligned} Q_{AB} = {} & \tfrac{1}{2} q_{0G}(x_B y_A - x_A y_B) + \tfrac{1}{6} q_{xG}(x_A + x_B)(x_B y_A - x_A y_B) \\ & + \tfrac{1}{6} q_{yG}(y_A + y_B)(x_B y_A - x_A y_B) + \tfrac{1}{12} q_{xxG}(x_A^2 + x_A x_B + x_B^2) \\ & \times (x_B y_A - x_A y_B) + \tfrac{1}{12} q_{yyG}(y_A^2 + y_A y_B + y_B^2)(x_B y_A - x_A y_B) \\ & + \tfrac{1}{24} q_{xyG}(2x_A y_A + x_A y_B + x_B y_A + 2x_B y_B)(x_B y_A - x_A y_B) \end{aligned} \tag{7}$$

For the piecewise-constant reconstruction, the value in a cell is treated as a constant q_{0G}; therefore, only the first line of the preceding equation is used. For the linear distribution, only the first three lines of the equations are used.

From the preceding equations, it needs only to search all the segments generated by the intersection between the two meshes to complete the remapping process. The successive line/cell scanning method is used to determine these segments [3].

D. Discussion of Numerical Stability

The present remapping method is focused on the construction of the boundary conditions of a grid block. In this sense, the accuracy and stability discussed in this paper is just about the boundary conditions. The method does not change the spatial scheme. Therefore, the accuracy and stability of the scheme in the computation, such as the Roe flux difference splitting (FDS) scheme (second-order accurate with third-order MUSCL interpolation) employed in the paper does not change.

With a series of one-dimensional and 2-D remapping test cases, Cheng and Shu [16] have proved that the accuracy of remapping is second order when based on the piecewise linear reconstruction and third order when based on the quadratic reconstruction.

The conservative remapping is developed initially for the moving grid or arbitrary Lagrangian–Eulerian applications. Many researchers have discussed the stability of different remapping methods [15,22]. Margolin and Shashkov [22] have shown that the stability of remapping can be defined as the remapped field bounded by the original field. They further proved that the stability can be preserved when 1) the positivity (sign preserving) can be guaranteed, and 2) the conservation of the whole interface can be guaranteed. In the present method, the global conservation of the remapping on the interface has already been proved. When the reconstruction is monotonic, no new peak value is created in the remapping. The remapped field should be naturally bounded. This is, of course, a strong constraint for the stability. For the sake of accuracy, the ENO and WENO strategies are incorporated instead of a strict monotonicity-preserving one. They are believed to be able to provide a weak guarantee for the monotonicity of the reconstruction, and hence for the stability of the remapping.

E. Verification of Conservative Remapping

In this section, remapping of scalar qualities between coarse and fine meshes is used to illustrate the advantage of the high-order remapping methods. The grid numbers are 30×20 and 81×91 on the coarse and fine sides of the interface, respectively. Although this is not required in the remapping algorithm, both grids are averagely spaced for the simplicity of this illustration. Take the density field as an example; the Gaussian distribution of the density on the coarse grid can be assumed:

$$\begin{aligned} \rho = {} & 1 + \exp\{-\ell n(1.002)[(x-0.5)^2 + (y-0.5)^2]/0.003^2\} \\ & x, y \in [0, 1] \end{aligned} \tag{8}$$

Figures 5 and 6 show the remapping of this distribution from the coarse grid onto the fine grid. The result of the first-order remapping shows an obvious stairlike effect. It means that the coarse grid cannot provide sufficient field details for the fine grid. Results of the second- and third-order remappings are much smoother. Comparing ENO with WENO reconstruction, WENO performs better on both second- and third-order remappings. Conclusively, third-order WENO remapping gives the best result but also costs the largest computational resources. Figure 6 shows the contours on both sides of the interface. The stairlike effect can be clearly seen in the first-order remapping. However, all the contour lines of higher-order remapping, both by ENO and WENO, match well with the original distribution on the coarse grid.

To test the method's capability of remapping the field with discontinuity, another distribution is assumed on the coarse mesh:

$$\rho = \begin{cases} 1.0 + \exp\{-\ell n(1.002)[(x-0.5)^2 + (y-0.5)^2]/0.003^2\} & x \in [0, 0.5], y \in [0, 1] \\ 2.0 + \exp\{-\ell n(1.002)[(x-0.5)^2 + (y-0.5)^2]/0.003^2\} & x \in [0.5, 1], y \in [0, 1] \end{cases} \tag{9}$$

The remapping results from the coarse grid to the fine grid are shown in Fig. 7. At the smooth region, the first-order remapping still shows a stairlike effect. As a comparison, the second-order and third-order remapping perform much better. The discontinuity is sharply captured without numerical oscillation. With the ENO and WENO strategies, the remapping preserves monotonicity and numerical stability very well.

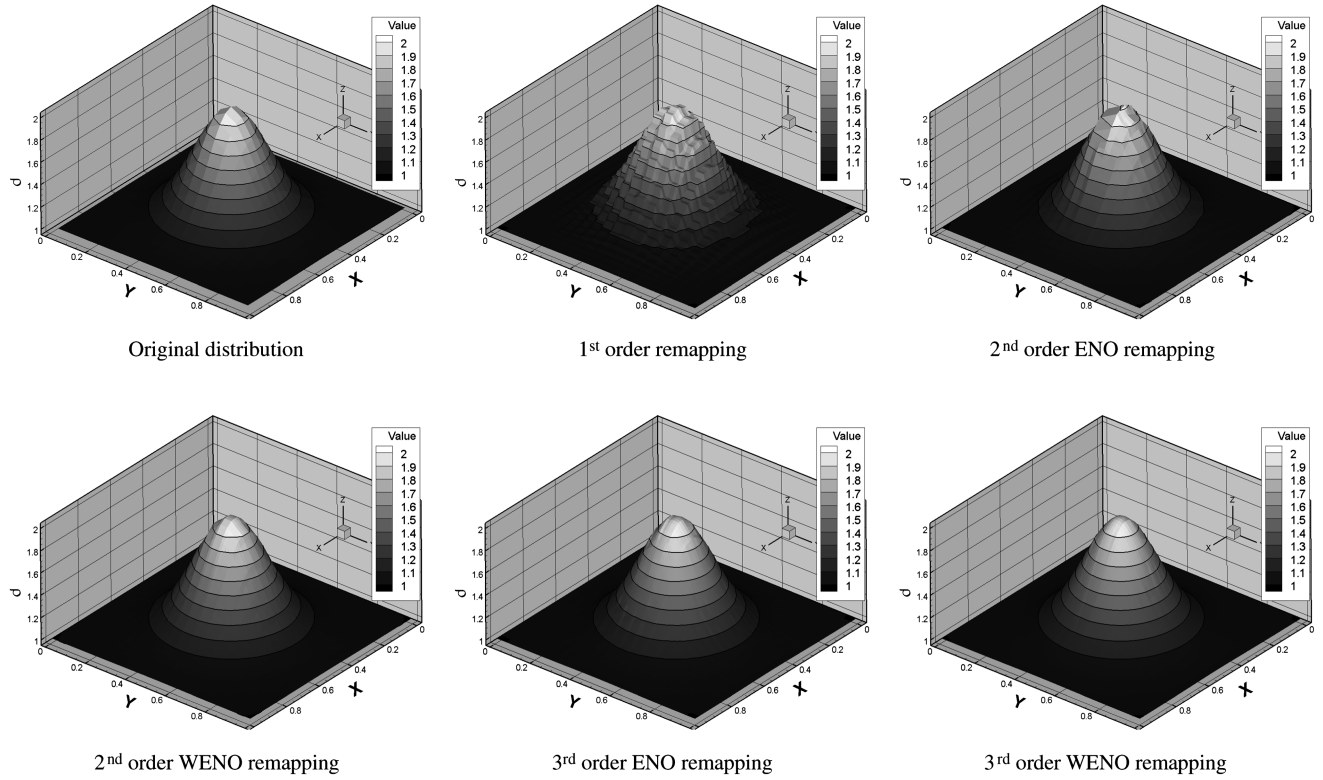

Original distribution | 1st order remapping | 2nd order ENO remapping

2nd order WENO remapping | 3rd order ENO remapping | 3rd order WENO remapping

Fig. 5 Remapping of smooth field from coarse mesh to fine meshes (3-D contour view).

From the quality of the results and the CPU time consumed, the second-order remapping with WENO strategy makes the best compromise in accuracy and efficiency, and it is recommended for the engineering applications.

III. Application to DLR-F4 Configuration with Mending Plate on Wing

A. Problem Description

To test the applicability and accuracy of the present approach in realistic aeronautical problems, the patched grid technique is applied to a challenging aerodynamic problem: simulation of the effects of a mending plate on the wing surface. The geometry model is a wing–body configuration with a rectangle mending plate patched on the upper surface of the wing. Resolving such geometry with a one-to-one matched grid approach would be extremely expensive, because the thickness of the mending plate used here is only 4 mm on a real Airbus A320 civil jet. The window-embedment technology as well as the patched grid technique are expected to provide a solution.

To better assess the accuracy of the methods, the DLR-F4 wing–body configuration is chosen as the baseline geometry. This configuration was the standard test case in the first AIAA Drag Prediction Workshop (DPW) [23] and has plenty of test data for the verification and calibration of numerical methods. To better reproduce the real problem, the DLR-F4 experimental model, for which the original span is 1.17 m, is magnified 20 times to the size of a realistic civil jet. The dimensions of the rectangle mending plate are 500 mm in the spanwise direction, 200 mm in the chordwise direction, and 4 mm in the protrusive thickness above the wing surface. All four edges are faced off by 15 deg. The mending plate is located at 32% of the half-span and 60% of the local chord length, and it has no sweepback angle. The geometry can be found in Fig. 8.

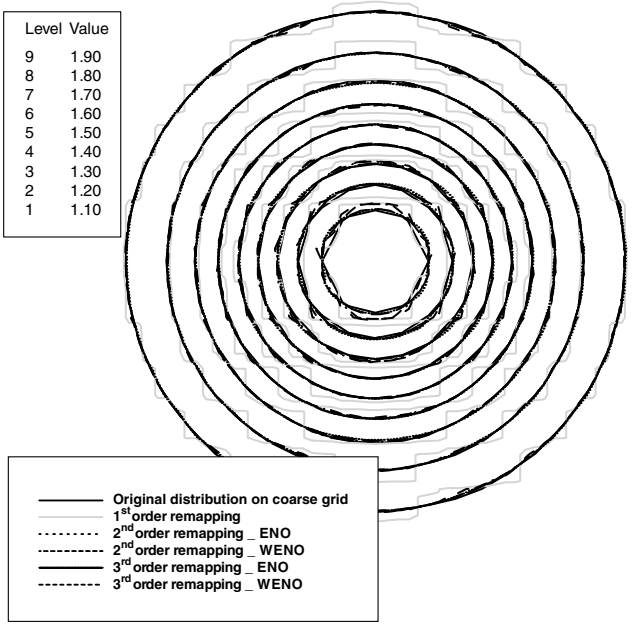

Fig. 6 Remapping of smooth field from coarse mesh to fine meshes (2-D contour view).

B. Numerical Method

The updated patched grid technique is developed based on, and implemented into, the in-house NSAWET code, which has been used for years on engineering simulations of realistic aircraft configurations. This finite volume code for the structural grid has integrated multiple spatial and time-advancing schemes and provides the users with several widely used turbulence models.

1. Spatial Schemes

In the present application, the Roe FDS scheme is employed for spatial discretization. The third-order MUSCL upwind bias interpolation is employed to ensure that the scheme is second-order accurate on nonuniform and curvilinear grid. The smooth and continuously derivable van Albada limiter is used to restrict the high-order spurious oscillation in the numerical solution.

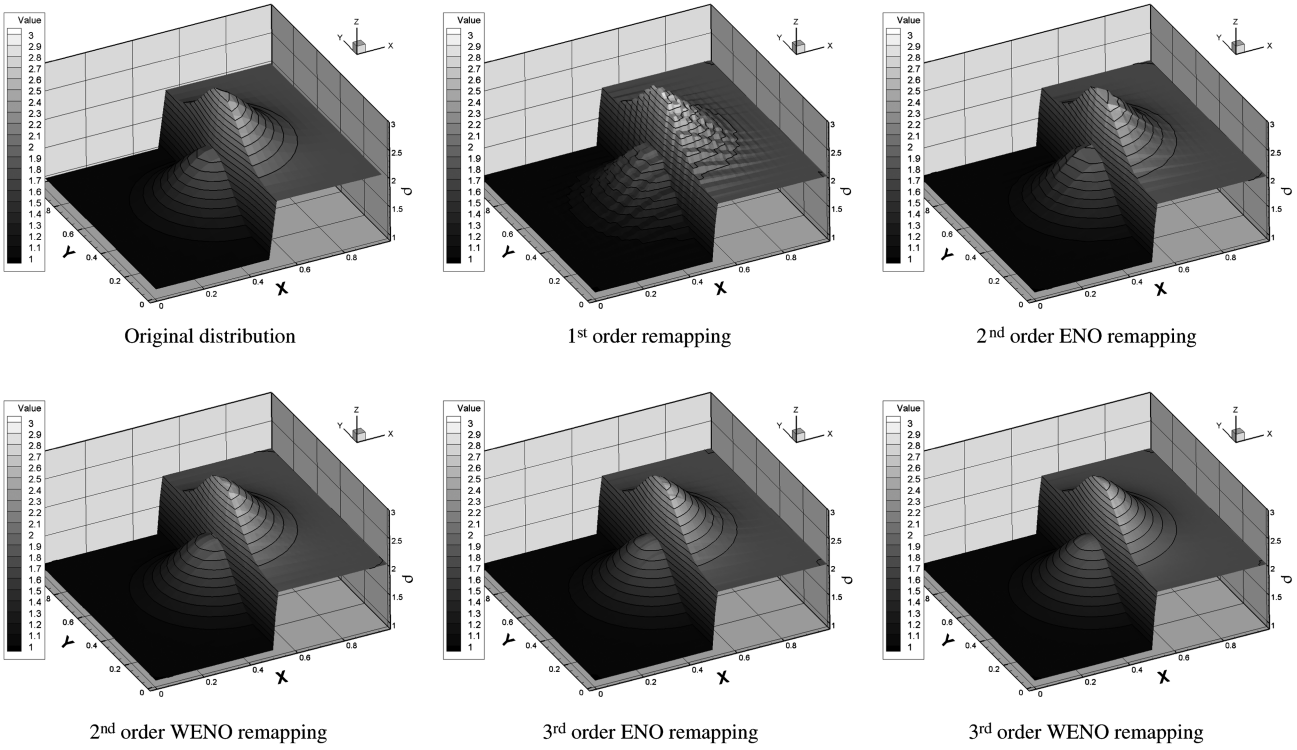

Fig. 7 Remapping of discontinuous field from coarse mesh to fine meshes.

For the patched grid, the Jameson cell-centered finite volumes scheme integrated in NSAWET is easy to maintain the flux conservation by direct remapping of the state vectors. However, for the Roe scheme, the conservative remapping method is first used to obtain the ghost cell values of each piece of the overlapped areas on the mismatched interfaces. The flux is then computed with the Riemann solver and, finally, the flux is summed up for a grid cell to get its total flux on the interface.

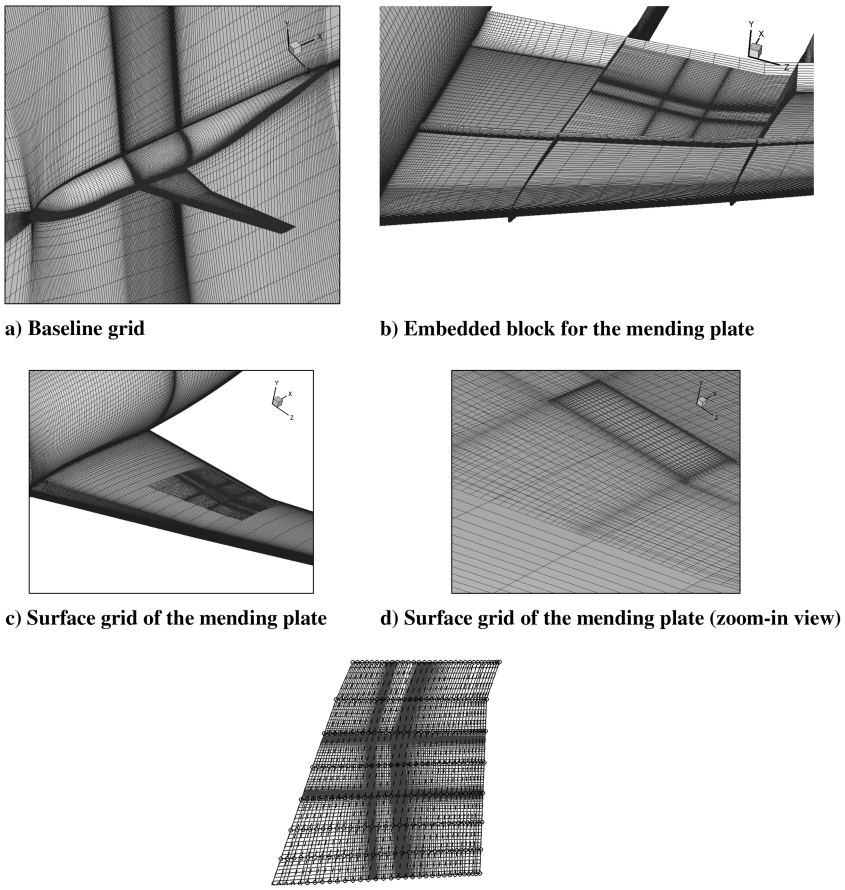

a) Baseline grid

b) Embedded block for the mending plate

c) Surface grid of the mending plate

d) Surface grid of the mending plate (zoom-in view)

e) Mismatched interface above the mending plate

Fig. 8 Grid of DLR-F4 wing–body configuration with mending plate.

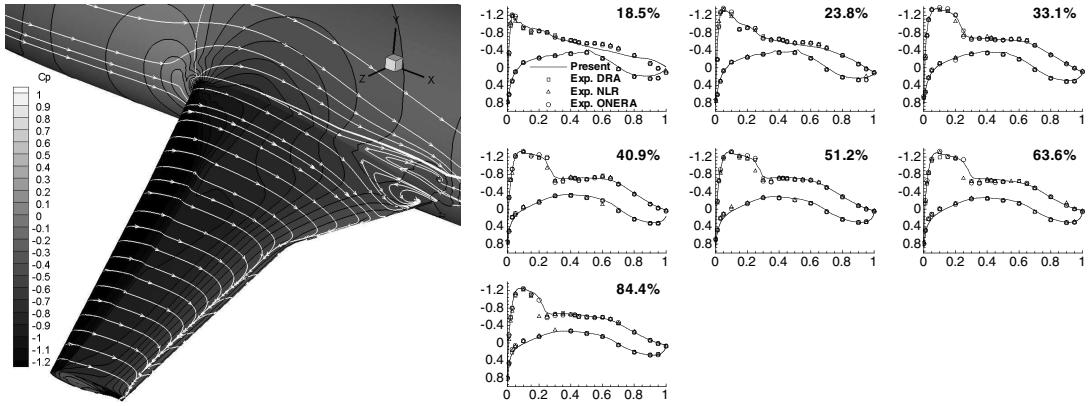

Fig. 9 Pressure distribution and surface streamlines of baseline configuration and comparisons of pressure distributions with test data for $Cl = 0.5$ (NLR denotes National Aerospace Laboratory of The Netherlands).

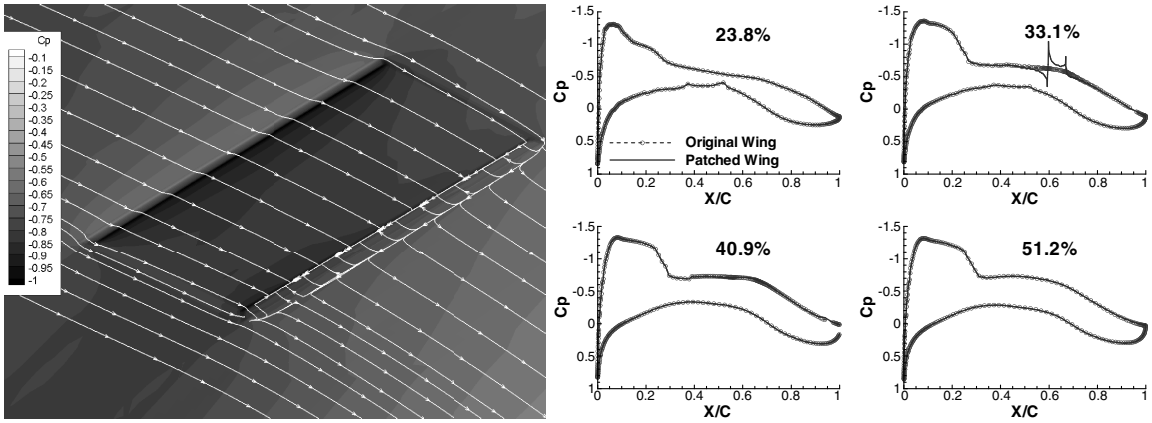

Fig. 10 Pressure distribution and surface streamline of repaired wing area and comparisons of pressure coefficient between original and mended wings.

2. Time-Advancing Schemes

The fully implicit lower–upper symmetric-Gauss–Seidel scheme is integrated as the time-stepping method for both Navier–Stokes (N–S) equations and the turbulence model equations in NSAWET. To achieve the second order of temporal accuracy in unsteady computation, the dual-time stepping is adopted.

3. Turbulence Models

In the present computation, the *k-g* model [24] is used for the turbulence stress closure. The model's equations are listed as follows. This model has three numerical advantages: no wall distance, simple source terms, and straightforward boundary conditions:

$$\frac{\partial(\rho k)}{\partial t} + \frac{\partial(\rho u_i k)}{\partial x_i} = \frac{\partial}{\partial x_i}\left[\left(\mu_l + \frac{\mu_t}{\sigma_k}\right)\frac{\partial k}{\partial x_i}\right] + P_k - \frac{\beta^* \rho^2 k^2}{R} \quad (10)$$

$$\frac{\partial(\rho g)}{\partial t} + \frac{\partial(\rho u_i g)}{\partial x_i} = \frac{\partial}{\partial x_i}\left[\left(\mu_l + \frac{\mu_t}{\sigma_g}\right)\frac{\partial g}{\partial x_i}\right] - \alpha\frac{\beta^* \rho g^3}{2R}P_k + \frac{\beta\rho^2 kg}{2R} - \left(\mu_l + \frac{\mu_t}{\sigma_g}\right)\frac{3\beta^*\rho kg}{R}\frac{\partial g}{\partial x_i}\frac{\partial g}{\partial x_i} \quad (11)$$

The eddy viscosity $\mu_t = \beta^* \rho k g^2$, and the constants are $\sigma_k \equiv \sigma_g \equiv \sigma_\omega = 2$, $\alpha = 5/9$, $\beta^* \equiv 0.09$, and $\beta = 0.075$. $R = \max(0.01\mu_l, \mu_t)$ is a limiter based on local eddy viscosity. The turbulent kinetic energy k and the turbulence transport variable g are both zero on the wall; the model's wall boundary condition is thus simple and of good numerical property. The solution of the model equations is decoupled from that of N–S equations. Second-order upwind scheme is used for spatial discretization. The accuracy and robustness of this model for civil aircraft application has been demonstrated in [4].

C. Grid Generation

The baseline grids of the DLR-F4 wing–body configuration can be downloaded from the website of the DPW workshop.[§] The grid selected for the present research is a multiblock structured grid generated by the DLR, German Aerospace Center (Fig. 8). The basic topology of the grid is *H-O*. An *H* grid extends to the far field, and an *O* grid covers the fuselage and the wing. To improve the grid quality, the wing is surrounded with a *C* grid block. The total grid points number is 3.1 million, and the normal height of the first layer cells on the solid surfaces is about 2×10^{-6} normalized by the semispan length.

According to the idea of window embedment [3], a fine-grid block is embedded into the *C* grid block of the wing to simulate the patched plate, as shown in Fig. 8b. In this procedure, a $55 \times 109 \times 91$-node (in the normal, chord, and spanwise directions, respectively) block is embedded into a window occupying a $28 \times 33 \times 8$ block in the wing grid. The embedded block has a reasonably high grid density in the chord and spanwise directions to describe the protrusive mending plate, as shown in Fig. 8c. The patched grid technique is used for flow information exchange on the interfaces of the embedded block. The baseline grid is very coarse in the embedment area. As shown in Fig. 8e, only two grid points of the baseline grid (dashed lines with circles) cover the range of the mending plate in the spanwise direction.

[§]Data available at ftp://cmb24.larc.nasa.gov/outgoing/DPW1 [retrieved May 2006].

Table 1 Comparisons of aerodynamic coefficients between the original wing and mended wing at different angles of attack (AOAs)

AOA	Configuration	C_l	C_d	$C_{d,p}$	$C_{d,f}$	M_z
0.4	Original wing	0.5092	0.03023	0.01890	0.01133	−0.1456
0.4	Mended wing	0.5086	0.03034	0.01900	0.01134	−0.1465
	Difference	−0.12%	+1.1 counts	+1.0 count	+0.1 count	−0.62%
1.2	Original wing	0.5973	0.03655	0.02540	0.01115	−0.1445
1.2	Mended wing	0.5981	0.03662	0.02550	0.01112	−0.1455
	Difference	+0.13%	+0.7 count	+1.0 count	−0.3 count	−0.69%

D. Baseline Configuration Computation

Results for the $C_l = 0.5$ case of baseline configuration are shown in Fig. 9. There were three sets of experimental data about this case [23]. Results of the present calculation match well with the data from the Defence Research Agency (DRA) and ONERA. The present drag coefficient is 0.0298 (with pressure drag 0.0185 and viscous drag 0.0113), about 0.0008 higher than the measured value, which is 0.029. The pressure distribution matches the measurement perfectly. In the present study, the main purpose is to estimate the increment of the drag caused by the patched plate on the wing. Such a systematic error will not affect the accuracy of the increment prediction.

E. Mended Wing Computation

The aerodynamic effects caused by the mending plate to the wing are studied. To exclude the influence of the local grid refinement in the window, both the baseline configuration and the mended wing configuration are studied by the window-embedment method. The results from the second-order WENO remapping method are discussed here first.

The results of the mended wing are shown in Fig. 10 and compared with those of the baseline configuration. At the 33.1% wingspan section, which is just at the midspan of the plate, the mending plate produces a sharp jump in the pressure distribution, as shown in

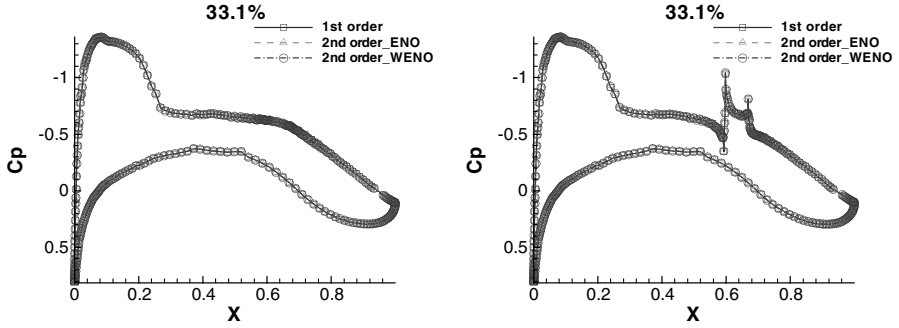

a) Original wing **b) Mended wing**

Fig. 11 Comparisons of surface pressure coefficients predicted by different remapping methods.

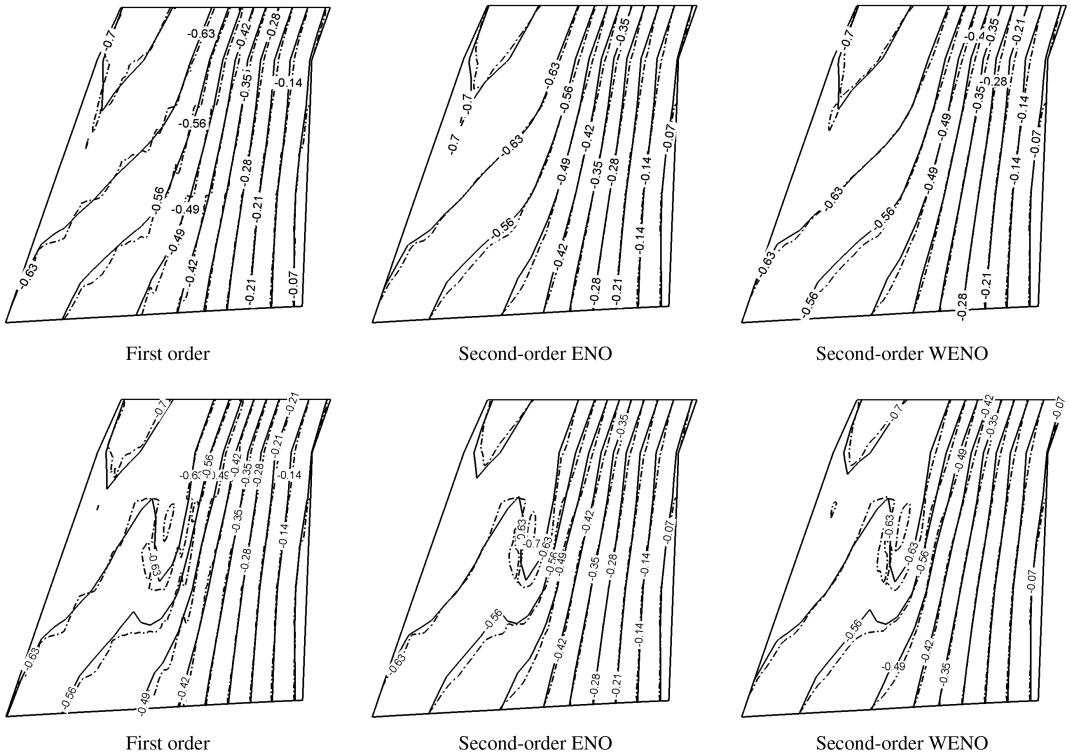

First order Second-order ENO Second-order WENO

First order Second-order ENO Second-order WENO

Fig. 12 Comparisons of pressure contours on both sides of the mismatched interface (upper: original wing; lower: mended wing).

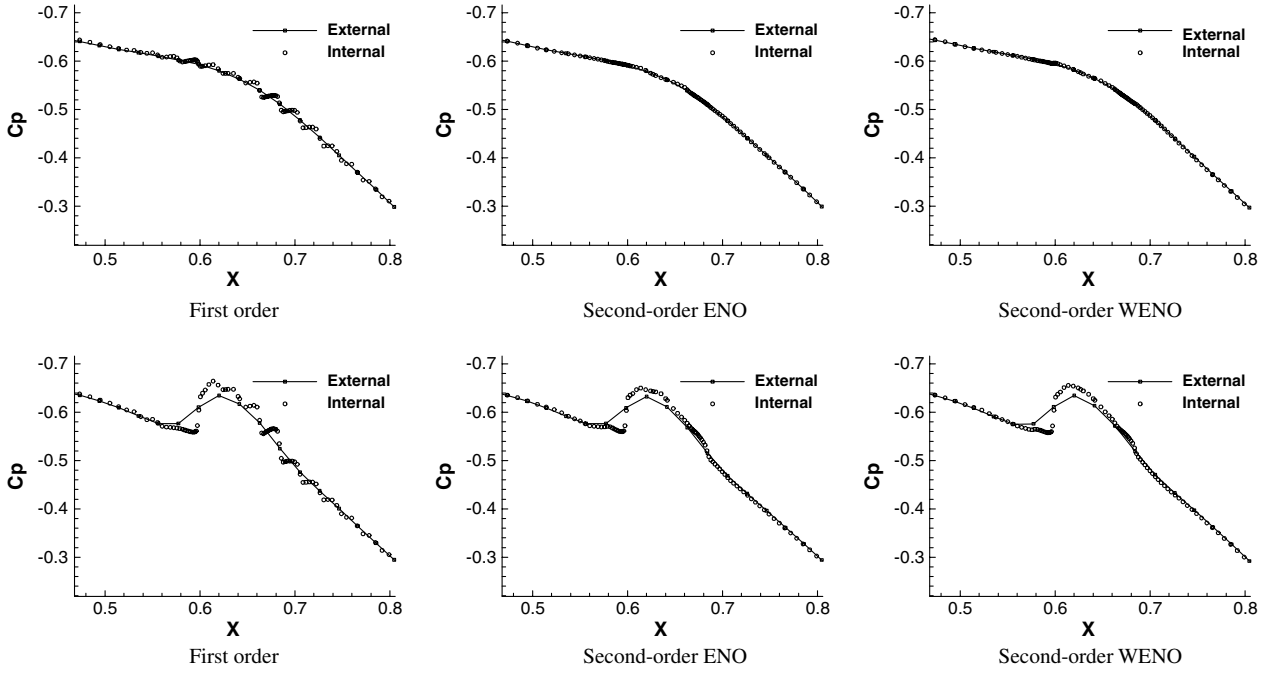

Fig. 13 Comparisons of pressure coefficients on both sides of the mismatched surface at 33.1% semispan location (upper: original wing; lower: mended wing).

Fig. 10. On other sections, which are outside the range of the plate, the results are almost identical to those of the original wing. The mending plate causes a small separation at its trailing edge, where it is like a backward stage to the flow. On the plate, the pressure coefficient is lower than that of the original wing, showing that the fluid is accelerated over the plate. This plateau of suction on the wing may increase the drag coefficient as the local normal direction is pointing rearward.

Two flow conditions are numerically simulated for both original and mended configurations. Lift and drag coefficients of the cases are listed in Table 1. Total drag coefficients of the mended wing are increased, mainly caused by the 0.7 to 1.1 counts (one count is equal to 0.0001 drag coefficient) increment in pressure drag. The variation of the total friction drag is trivial (about ± 0.2 counts).

F. Comparison of Remapping Methods

The first-order and second-order ENO and WENO remapping methods are compared for the mending plate computation. The results for the $Ma = 0.75$, $\alpha = 0.4^\circ$ case are compared.

Figure 11 shows the influence of the remapping accuracy on the surface pressure distribution. The C_p results for the 33.1% spanwise section are compared. The results by the three methods are not distinguishable.

The difference of the grid density inside and outside the window is very large. On the side of the baseline grid, the interface grid has only 33×8 nodes, and on the embedded grid side, the interface grid has 109×91 nodes. The remapping methods show great differences on the predicted local flow details. Figure 12 shows the pressure contours on both sides of the mismatched interface. Figure 13 shows the pressure distributions on the mismatched interface at the 33.1% spanwise location.

Distributions predicted by the second-order remapping methods are quite smooth. Results of ENO and WENO methods show little difference. However, the results of the first-order remapping show some annoying stairlike jumps.

For the original wing configuration, ENO and WENO are both excellent, as the flow information is smooth. When a plate is mended on the wing, sharp pressure discontinuity occurs because of the leading edge of the plate. The ENO and WENO remapping methods show their importance here. The pressure jump is well resolved in the window without any overshot or spurious vibration. Outside the window, the pressure is dramatically smeared in the coarse grid. If the pressure jump is important to the flow outside the window, the baseline grid should be refined at the location of the plate. However, if it is not important, the grid density difference here means the saving of the baseline grid nodes.

G. Comparison of Baseline Computation With and Without Window Embedment

In Table 2, the flow coefficients are compared between the computations with and without window embedment for the local grid refinement for the baseline configuration. The differences in C_l and C_d are only 0.04% and 0.2 counts, respectively. The surface pressure distributions are also compared at three locations in Fig. 14. It is clear that the local grid refinement and the patched grid treatment introduced by the window embedment have only negligible influence on the results. The drag increment predicted in Table 1 is again proved to be solely caused by the mending plate. The patched grid itself does not cause any artificial numerical effect. The accuracy of the patched grid technique is thus illustrated.

IV. Conclusions

The patched grid technique in the window-embedment approach is improved with higher-order conservative remapping. With the high-order polynomial reconstruction, the criteria of stencil selection, and

Table 2 Comparisons of aerodynamic coefficients for baseline configuration, with and without window embedment

AOA	Window embedment	C_l	C_d	$C_{d,p}$	$C_{d,f}$	M_z
0.4	With	0.5092	0.03023	0.01890	0.01133	−0.1456
0.4	Without	0.5090	0.03021	0.01886	0.01135	−0.1460
	Difference	0.04%	0.2 counts	0.4 counts	0.2 count	0.3%

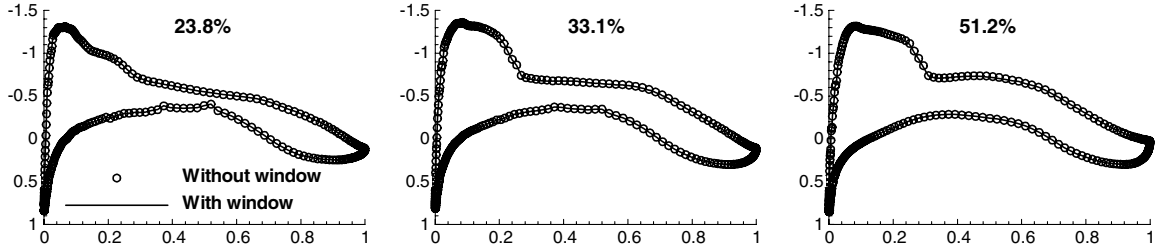

Fig. 14 Comparisons of surface pressure coefficients predicted for baseline configuration, without and with the window-embedment grid (23.8% section: inboard of window; 33.1% section: in window; 51.2% section: outboard of window).

the ENO and WENO strategies, the method achieves higher accuracy in exchanging the flow information on the mismatched grid interface. The fidelity, resolution, and smoothness of the remapping are obviously improved. The favorable feature of conservation is well preserved. The robustness and stability of the present method are also satisfying. The second-order remapping with WENO is recommended for its best compromise in numerical accuracy and computational costs.

The improved patched grid technique shows good accuracy, applicability, and robustness in engineering computations. High-order remapping has been successfully employed to capture the delicate difference in the aerodynamics performance caused by the tiny change in geometry.

Acknowledgments

The support from Airbus S.A.S. is greatly appreciated. The work is also supported by the National Natural Science Foundation of China projects 10972120 and 10932005. This work is part of the collaboration between Tsinghua University and Airbus S.A.S.

References

[1] Mary, I., and Sagaut, P., "Large Eddy Simulation of Flow Around an Airfoil Near Stall," *AIAA Journal*, Vol. 40, No. 6, 2002, pp. 1139–1145. doi:10.2514/2.1763

[2] Deck, S., "Numerical Simulation of Transonic Buffet over a Supercritical Airfoil," *AIAA Journal*, Vol. 43, No. 7, 2005, pp. 1556–1566. doi:10.2514/1.9885

[3] Chen, H. X., and Fu, S., "Navier–Stokes Simulations for Transport Aircraft Wing/Body High-Lift Configurations," *Journal of Aircraft*, Vol. 40, No. 5, 2003, pp. 883–890. doi:10.2514/2.6878

[4] Zhang, Y. F., Chen, H. X., Fu, S., Duan, Z. Y., and Qian, R. Z., "Computations of a Twin-Engine Civil Transporter Using Window Embedment Grid Technique," AIAA Paper 2008-0169, Jan. 2008.

[5] Wei, H., and Chen, Y. S., "Numerical Simulation Using Conservative Patched Grid Interface for Multiblock Complex Flows," AIAA Paper 2000-0397, Jan. 2000.

[6] Rai, M. M., "A Conservative Treatment of Zonal Boundaries for Euler Equation Calculations," *Journal of Computational Physics*, Vol. 62, No. 2, 1986, pp. 472–503. doi:10.1016/0021-9991(86)90141-5

[7] Walters, R. W., Thomas, J. L., and Switzer, G. F., "Aspects and Applications of Patched Grid Calculations," AIAA Paper 1986-1063, May 1986.

[8] Thomas, J. L., Walters, R. W., Reu, T., Ghaffari, F., Weston, R. P., and Luckring, J. M., "Application of a Patched-Grid Algorithm to the F/A-18 Forebody-Leading-Edge Extension Configuration," *Journal of Aircraft*, Vol. 27, No. 9, 1990, pp. 749–756. doi:10.2514/3.45934

[9] Lerat, A., and Wu, Z. N., "Stable Conservative Multidomain Treatments for Implicit Euler Solvers," *Journal of Computational Physics*, Vol. 123, No. 1, 1996, pp. 45–64. doi:10.1006/jcph.1996.0004

[10] Benkenida, A., Bohbot, J., and Jouhaud, J. C., "Patched Grid and Adaptive Mesh Refinement Strategies for the Calculation of The Transport Of Vortices," *International Journal for Numerical Methods in Fluids*, Vol. 40, No. 7, 2002, pp. 855–873. doi:10.1002/fld.378

[11] Yang, H., Nuernberger, D., Nicke, E., and Weber, A., "Numerical Investigation of Casing Treatment Mechanisms with a Conservative Mixed-Cell Approach," ASME Turbo Expo 2003, American Soc. of Mechanical Engineers Paper GT2003-38483, Fairfield, NJ, June 2003.

[12] Esquieu, S., "Numerical Simulation and Drag Extraction Using Patched Grid Calculations," AIAA Paper 2003-1238, Jan. 2003.

[13] Esquieu, S., "Aircraft Drag Extraction from Patched Grid Computations," AIAA Paper 2003-3659, June 2003.

[14] Chen, H. X., Fu, S., and Li, F. W., "Navier–Stokes Simulations for Transport Aircraft Wing–Body Combinations with Deployed High-Lift Systems," AIAA Paper 2003-4077, June 2003.

[15] Wang, Y. J., and Zhao, N., "A Kind of Rezoning (Remapping) Algorithms Based on ENO Interpolation," *Chinese Journal of Computational Physics*, Vol. 21, No. 4, 2004, pp. 329–334 (in Chinese). doi:CNKI:SUN:JSWL.0.2004-04-008

[16] Cheng, J., and Shu, C. W., "A High Order Accurate Conservative Remapping Method on Staggered Meshes," *Applied Numerical Mathematics*, Vol. 58, No. 7, 2008, pp. 1042–1060. doi:10.1016/j.apnum.2007.04.015

[17] Bryson, S., and Levy, D., "High-Order Central WENO Schemes for Multidimensional Hamilton–Jacobi Equations," *SIAM Journal on Scientific Computing*, Vol. 41, No. 4, 2003, pp. 1339–1369. doi:10.1137/S0036142902408404

[18] Philip, W. J., "First- and Second-Order Conservative Remapping Schemes for Grids in Spherical Coordinates," *Monthly Weather Review*, Vol. 127, No. 9, 1999, 2204–2210. doi:10.1175/1520-0493(1999)127<2204:FASOCR>2.0.CO;2

[19] Zhang, Y. T., and Shu, C. W., "High-Order WENO Schemes for Hamilton-Jacobi Equations on Triangular Meshes," *SIAM Journal on Scientific Computing*, Vol. 24, No. 3, 2003, pp. 1005–1030. doi:10.1137/S1064827501396798

[20] Liu, Y., "Central Schemes on Overlapping Cells," *Journal of Computational Physics*, Vol. 209, No. 1, 2005, pp. 82–104. doi:10.1016/j.jcp.2005.03.014

[21] Mao, J. F., "Arbitrary Lagrangian–Eulerian Method Based on Adaptive Structure Grids," M.S. Thesis, College of Aerospace Engineering, Nanjing Univ. of Aeronautics and Astronautics, Nanjing, PRC, Jan. 2007 (in Chinese).

[22] Margolin, L. G., and Shashkov, M., "Second-Order Sign-Preserving Conservative Interpolation (Remapping) on General Grids," *Journal of Computational Physics*, Vol. 184, No. 1, 2003, pp. 266–298. doi:10.1016/S0021-9991(02)00033-5

[23] Levy, D. W., Zickuhr, T., Vassberg, J., Agrawal, S., Wahls, R. A., Pirzadeh, S., and Hemsch, M. J., "Summary of Data from the First AIAA CFD Drag Prediction Workshop," AIAA Paper 2002-0841, Jan. 2002.

[24] Xiao, Z. X., Chen, H. X., Fu, S., and Li, F. W., "Numerical Simulation of High Angle of Attack Transonic Flows About a Complete Aircraft Configuration with *k-g* Model," *Journal of Aircraft*, Vol. 42, No. 2, 2005, pp. 462–470. doi:10.2514/1.6821